The globular cluster system of the Auriga simulations

Timo L. R. Halbesma[1]⋆, Robert J. J. Grand[1], Facundo A. Gómez[2,3], Federico Marinacci[4],
Rüdiger Pakmor[1], Wilma H. Trick[1], Philipp Busch[1], Simon D. M. White[1]

[1] *Max-Planck-Institut für Astrophysik, Karl-Schwarzschild-Str. 1, 85741 Garching, Germany*

[2] *Instituto de Investigación Multidisciplinar en Ciencia yTecnología, Universidad de La Serena, Raúl Bitrán 1305, La Serena, Chile*

[3] *Departamento de Física y Astronomía, Universidad de La Serena, Av. Juan Cisternas 1200 N, La Serena, Chile*

[4] *Department of Physics & Astronomy, University of Bologna, via Gobetti 93/2, 40129 Bologna, Italy*

ABSTRACT

We investigate whether the galaxy and star formation model used for the Auriga simulations can produce a realistic globular cluster (GC) population. We compare statistics of GC candidate star particles in the Auriga haloes with catalogues of the Milky Way (MW) and Andromeda (M31) GC populations. We find that the Auriga simulations do produce sufficient stellar mass for GC candidates at radii and metallicities that are typical for the MW GC system (GCS). We do observe varying mass-ratios of the simulated GC candidates relative to the observed mass in the MW and M31 GC systems for different bins of galactocentric radius-metallicity ($r_{\rm gal}$-[Fe/H]). This may imply that different values for the combined product of the bound cluster formation efficiency and the GC disruption rate are needed. Overall, the Auriga simulations produce GC candidates with higher metallicities than the MW and M31 GCS and they are found at larger radii than observed. Bound cluster formation efficiencies higher than ten percent are needed for the metal-poor GC candidates, and those within the Solar radius should experience negligible destruction rates. GC candidates in the outer halo, on the other hand, should either have low formation efficiencies, or experience high mass loss for the Auriga simulations to produce a GCS that is consistent with that of the MW or M31. Finally, the scatter in the metallicity as well as in the radial distribution between different Auriga runs is considerably smaller than the differences between that of the MW and M31 GCSs. The Auriga model is unlikely to give rise to a GCS that can be consistent with both galaxies.

Key words: galaxies: formation – galaxies: star clusters: general.

1 INTRODUCTION

Globular star clusters (GC)s are old, bright, and ubiquitous. Various properties of GC systems (GCS) show correlations with their host galaxies. GCSs are believed to retain information about the galactic (gas) conditions at their times of formation. Thus they could offer a unique insight into the (chemodynamical) evolution of their parent galaxies, if the formation and evolution of GCs- and GC systems themselves is adequately understood. However, despite decades of research (the extensive literature on GCs is summarised in several books and review articles, e.g. Harris 1991; Harris 2001; West et al. 2004; Brodie & Strader 2006; Gratton et al. 2012; Kruijssen 2014; Forbes et al. 2018), consensus on an exhaustive picture of the formation of GCs is yet to be reached.

The literature offers a wealth of formation scenarios. Peebles & Dicke (1968) and Peebles (1984) argue that GCs form as the earliest bound structures in the Universe (i.e. prior to formation of

the main galaxy), noting that the Jeans length and mass shortly after recombination is consistent with typical GC masses and sizes. Diemand et al. (2005) and Boley et al. (2009) argue that (the blue subpopulations of) GCs form in radially biased dark matter (DM) halos at high redshift. Other recent hypotheses of GC formation prior to collapse of the proto-galaxy include formation in colliding supershells (Recchi et al. 2017), in supersonically induced gaseous objects (Chiou et al. 2019), or in high-speed collisions of dark matter subhaloes (Madau et al. 2019). Boylan-Kolchin (2017) suggests that (the blue subpopulation of) GCs could form in high density regions along the cosmic filament before or during collapse.

Other models also date GCs formation during formation of the proto-galaxy itself, for example as a result of thermal instabilities in hot gas-rich haloes (Fall & Rees 1985, also see the discussions in Kang et al. 1990). Alternative formation triggers are also explored, such as (other causes of) shock compression, or cloud-cloud colisions (e.g. Gunn 1980; Murray & Lin 1992; Harris & Pudritz 1994; Vietri & Pesce 1995; Larson 1996; Cen 2001).

Yet another hypothesis is that star cluster formation is triggered

⋆ E-mail: Halbesma@MPA-Garching.MPG.DE

by major gas-rich (spiral) galaxy mergers (Schweizer 1987; Ashman & Zepf 1992), which is naturally expected within the framework of hierarchical assembly. One testable prediction of this scenario is the formation of young clusters in interacting and merging galaxies, which has been observed and are found to show remarkable similarities with GCs in the Milky Way (MW) (e.g. Whitmore & Schweizer 1995; Holtzman et al. 1996; Zepf et al. 1999; Whitmore et al. 1999). Moreover, modelling efforts of this framework yield GC (sub)populations consistent with various observables (e.g. Muratov & Gnedin 2010; Choksi et al. 2018), and the recent numerical simulation of an isolated dwarf-dwarf merger executed at very high resolution (baryonic mass $m_b \sim 4 M_\odot$; softening $\epsilon = 0.1$ pc) produces star clusters that could be GC progenitors (Lahén et al. 2019).

As for the formation timeline, the scenarios (and flavours thereof) of Fall & Rees (1985) and Ashman & Zepf (1992) are intertwined because accretion and mergers continuously occurs during the hierarchical build-up of galaxies. Various (other) hierarchical formation channels thus combine different aspects of the aforementioned paradigms, such as GC formation in (small) galactic disks before they are accreted onto an assembling galaxy (e.g. Côté et al. 2000, 2002; Beasley et al. 2002; Gnedin 2003). We refer to Gnedin et al. (2001) for a scoreboard of GC formation models compared to observations of the MW GCSs.

An idea that has recently been studied extensively is the hypothesis that the formation mechanisms of young massive clusters (YMCs, see Portegies Zwart et al. 2010, for a review) and GCs are the same. The proximity of YMCs in the local Universe allows to study these processes with a level of detail that cannot be achieved for GCs at high redshifts. In this framework, differences between both classes of objects are caused by nearly a Hubble time of (dynamical) evolution (e.g. Spitzer 1987). This picture is based on observed similarities between YMCs and GCs (e.g. Holtzman et al. 1992; Whitmore et al. 1999) and strengthened by observations of gravitationally lensed objects at high redshifts ($z = 2 - 6$). These sources have properties reminiscent of (local) YMCs and may be GC progenitors at times of formation (Vanzella et al. 2017; Johnson et al. 2017). The modelling work by Kruijssen et al. (2011, 2012); Kruijssen (2015) is now incorporated into cosmological zoom simulations and shows promising results (Pfeffer et al. 2018; Kruijssen et al. 2019).

The (mass) resolution of cosmological zoom simulations has reached the mass range populated by GCs, and the gravitational force softening can be as low several parsec. A number of groups can thus incorporate formation of (globular) star clusters into their high-resolution hydrodynamical simulations. Ricotti et al. (2016) ran parsec scale simulations of the high-redshift universe prior to reionization (the simulations stop at $z = 9$), Li et al. (2017) implement a new subgrid model for star (cluster) formation and run simulations that reach $z = 3.3$, and the run of Renaud et al. (2017) reaches $z = 0.5$. Kim et al. (2018) find that mergers can push gas to high density that quickly forms clustered stars that end up tightly bound by the end of the simulation. A somewhat different approach couples semi-analytical models to DM-only simulations (Muratov & Gnedin 2010; Li & Gnedin 2014; Choksi et al. 2018; Choksi & Gnedin 2019b,a), as is done in the work by El-Badry et al. (2019).

In this work we use state of the art simulations that produce realistic spiral galaxies (MW analogues) at redshift zero for which several global properties are consistent with the observations. The question thus naturally arises whether the star formation histories of the simulations give rise to a GCS similar to the MW and/or Andromeda (M31) GCSs. In particular, we use the Auriga simulations (Grand et al. 2017, hereafter G17), further described in Section 2.

We investigate whether the star formation model implemented produces metallicity, radial, and metallicity-radial distributions that are consistent with the MW and/or M31 GCSs, and whether the model produces enough stellar mass with the right properties to allow for formation efficiencies lower than unity and the expected (dynamical) mass loss over the cluster lifetime (not modelled explicitly in this study).

The plan of the paper is as follows. We summarise the relevant characteristics of the Auriga simulations in section 2, followed by a summary of the observations of the MW and M31 GCSs in section 3 that we use to compare our simulations to in section 4. We discuss our findings in section 5 to come to our conclusions in section 6.

2   THE AURIGA SIMULATIONS

We use the Auriga simulations (G17), a suite of high-resolution cosmological zoom simulations of MW analogues. The MW-mass selected initial conditions were selected from the EAGLE DM only box, see G17 for details. The simulations are performed with the AREPO code (Springel 2010; Pakmor et al. 2016) that solves the magnetohydrodynamical equations on a moving mesh.

The galaxy formation model includes primordial and metal-line cooling with self-shielding corrections. Reionization is completed at redshift six by a time-varying spatially uniform UV background (Faucher-Giguère et al. 2009; Vogelsberger et al. 2013). The interstellar medium (ISM) is described by an equation of state for a two-phase medium in pressure equilibrium (Springel & Hernquist 2003): cold clouds embedded in a hot ambient medium, whose mass and energy densities are described by processes important for star formation, such as the condensation of cold clouds and the photoevaporation of clouds. Stars form stocastically in thermally unstable gas with a density threshold of $n = 0.13 \, \text{cm}^{-3}$, and consecutive stellar evolution is accounted for. The channel for energetic stellar feedback is from non-local type II supernovae (SN), which is modelled with wind particles (Marinacci et al. 2014; G17). Galactic winds enrich the ISM with metals from SNIa, SNII, and asymptotic giant branch (AGB) stars (Vogelsberger et al. 2013). Supermassive black holes grow via Bondi–Hoyle–Lyttleton accretion (Bondi & Hoyle 1944; Bondi 1952), and feedback from the active galactic nuclei has a low-accretion and high-accretion mode (radio and quasar) (Springel et al. 2005; Marinacci et al. 2014; G17). Finally, the simulations follow the evolution of a magnetic field of 10^{-14} (comoving) G seeded at $z = 127$ (Pakmor & Springel 2013; Pakmor et al. 2014).

This model was tailored to the AREPO code and calibrated to reproduce key observables of galaxies, such as the history of the cosmic star formation rate density, the stellar mass to halo mass relation, and galaxy luminosity functions. The galaxy formation model produces realistic spiral galaxies at redshift zero that match observations such as sizes, morphologies (G17), HI disc properties (Marinacci et al. 2017), and the diversity of accreted stellar halo properties (Monachesi et al. 2019). Furthermore, the simulations are able to reproduce major Galactic components, such as the chemical thin/thick disc dichotomy (Grand et al. 2018) and the recently discovered *Gaia* Sausage (Fattahi et al. 2019). They are thus a large set of detailed simulations similar enough to the Galaxy to make predictions for the GC population properties of the MW and M31.

The Auriga suite has a fiducial baryonic mass resolution $m_b = 5 \times 10^4 \, M_\odot$, with gravitational softening of collissionless particles $\epsilon = 369$ pc. Simulations at this resolution are referred to as

level 4 (L4). Selected initial condition runs are acompanied by the lower (higher) resolution level L5 (L3). The resolution for these levels is $m_b = 4 \times 10^5$ M$_\odot$ with $\epsilon = 738$ pc, and $m_b = 6 \times 10^3$ M$_\odot$ with $\epsilon = 184$ pc, respectively. The mass resolution of the Auriga simulations is thus close to the characteristic peak mass of the lognormal GC mass distribution of 10^5 M$_\odot$(Harris 1991), although the gravitational softening is two orders of magnitudes larger than typical GC radii of several parsec. High-density gaseous regions are thus not expected to produce surviving stellar clumps with masses and radii consistent with GCs because such objects would numerically disperse, even in the highest-resolution runs. On the other hand, we can investigate (statistical) properties of age-selected GC candidates because each star particle represents a single stellar population with a total mass that could be consistent with one GC. This means that their formation sites and that of a real-world GC may be consistent.

3 OBSERVATIONAL DATA

We describe the observations of the MW GCS in Section 3.1, and of the M31 GCS in Section 3.2

3.1 Milky Way

Harris (1996, 2010 edition; hereafter H96e10) provides a catalogue[1] of the MW GCS that contains properties of 157 GCs. The authors initially estimated the number of GCs in the MW GCS to be 180 ± 10, thus, their catalogue to be ~85% complete. However, an additional 59 GCs are claimed to have been discovered by various authors. The total number of GCs in the MW might add up to 216 with recent estimates now anticipating an additional thirty GCs yet to be discovered (e.g. Ryu & Lee 2018, and references therein). We still use data from the Harris catalogue, but caution that it may (only) be 50-70% complete. Specifically, the relevant data fields that we use from H96e10 are the metallicity [Fe/H], the Galactic distance components X, Y, and Z (in kpc)[2], and absolute magnitude in the V band, M_V. We use the V band magnitude to calculate mass-estimates by assuming $M_{V,\odot} = 4.83$ and a mass to light ratio $M/L_V = 1.7$ M/L$_\odot$, the mean for MW clusters (McLaughlin & van der Marel 2005). We supplement the catalogue with age-estimates from isochrone fits to stars near the main-sequence turnoff in 55 GCs (VandenBerg et al. 2013, hereafter V13).

3.2 Andromeda

The fifth revision of the revised Bologna catalogue (RBC 5, last updated August, 2012) is the latest edition of three decades of systematically collecting integrated properties of the GCS of M31 (Galleti et al. 2004, and references therein). One contribution to RBC 5 is the work by Caldwell et al. (2011, hereafter C11), subsequently updated by Caldwell & Romanowsky (2016, hereafter CR16).

C11 and CR16 present a uniform set of spectroscopic observations calibrated on the MW GCS of the inner 1.6° (~21) kpc that is believed to be 94% complete. GCs in the outer stellar halo, up to

$r_{\rm proj} \sim 150$ kpc, are observed in the Pan-Andromeda Archaeological Survey (PAndAS, Huxor et al. 2014, hereafter H14), but see also Veljanoski et al. (2014) and Mackey et al. (2019). H14 presents the discovery of 59 new GCs and publishes updates to RBC 5. The work of H14 is incorporated in the latest public release[3] of the C11 dataset, further revised by CR16. We use CR16 because it is the most recent aggregated dataset of M31's GCS that contains properties of interest for our study and it includes GCs in the inner region and in the outer halo. The relevant fields in the CR16 dataset that we use are the age, metallicity, and the mass-estimate[4]. Radii are calculated from RA and DEC, further discussed in Sec. 3.4.

3.3 Age-estimates

The top panel of Figure 1 shows a histogram of the age-estimates of the 55 MW GCs in V13 and 88 GCs in M31 for which age-estimates are available in CR16. The mean age of the MW GCs in this data set is 11.9 ± 0.1 Gyr and the dispersion is 0.8 Gyr. Furthermore, only one of the 55 GC age-estimates is below 10 Gyr. The M31 GCS has a mean age of 11.0 ± 0.2 Gyr with a dispersion of 2.2 Gyr, and 24 GCs have age-estimates below 10 Gyr with a minimum age of 4.8 Gyr. Based on these data, we find that the age distributions of the MW and M31 GCSs are not statistically consistent. Moreover, the MW appears to host a GCS that is somewhat older than that of M31. This is somewhat surprising given that M31 is generally considered to be earlier type than the MW meaning that an older stellar population would be naively expected. However, we do caution that both data sets are incomplete and the age measurements have large uncertainties (of $1 - 2$ Gyr). On the other hand, the magnitude of the uncertainty is insufficient to explain the low-age tail in M31.

3.4 Radial distribution

The bottom panel of Figure 1 shows the radial distribution of the MW and M31 GCS. We divide the radii of M31 by its virial radius[5] $r_{\rm vir,M31} = 299$ kpc and multiply by $r_{\rm vir,MW} = 261$ kpc to account for the different intrinsic sizes of both galaxies, adopting the values and cosmology from Patel et al. (2017). Values for $r_{\rm gal}$ are readily available in H96e10 (assuming $r_\odot = 8.0$ kpc), but the galactocentric radius of GCs in M31 is not available in CR16. Therefore, we follow Wang et al. (2019, section 4.1) to calculate the projected radius $r_{\rm proj}$ from the observed positions, adopting M31's central position from the NASA Extragalactic Database[6] $(\alpha_0, \delta_0) = (0^{\rm h}42^{\rm m}44.35^{\rm s}, +41°16'08.63")$ and distance $D_{\rm M31} = 780$ kpc (McConnachie et al. 2005; Conn et al. 2012). We calculate $r_{\rm gal}$ as 'average deprojected distance' $r_{\rm gal} = r_{\rm proj} \times (4/\pi)$.

The solid lines show the distributions using all available data (because the sky coordinates are known for each GC), while the subset for which age-estimates are available is indicated using dotted lines. The latter shows a narrower range of radii than the full data set: it appears that few age-estimates are available for the innermost (< 1 kpc) GCs, and none for those beyond roughly twenty kpc (the halo GCs). We compare both distributions of the full data set (solid

---

[1] See https://www.physics.mcmaster.ca/Fac_Harris/mwgc.dat

[2] In a Sun-centered coordinate system: X points toward Galactic center, Y in direction of Galactic rotation, and Z toward the North Galactic Pole. We calculate the galactocentric radius $r_{\rm gal} = \sqrt{(X - r_\odot)^2 + Y^2 + Z^2}$, assuming the solar radius $r_\odot = 8$ kpc.

[3] Last revised 23 Sep 2015, see https://www.cfa.harvard.edu/oir/eg/m31clusters/M31_Hectospec.html

[4] The authors assumed $M/L_V = 2$ independent of [Fe/H]

[5] $r_{\rm vir}$ is the radius in a spherical 'top-hat' perturbation model at which the average density reaches an overdensity of $\Delta_{\rm vir} = 357$ times the background density
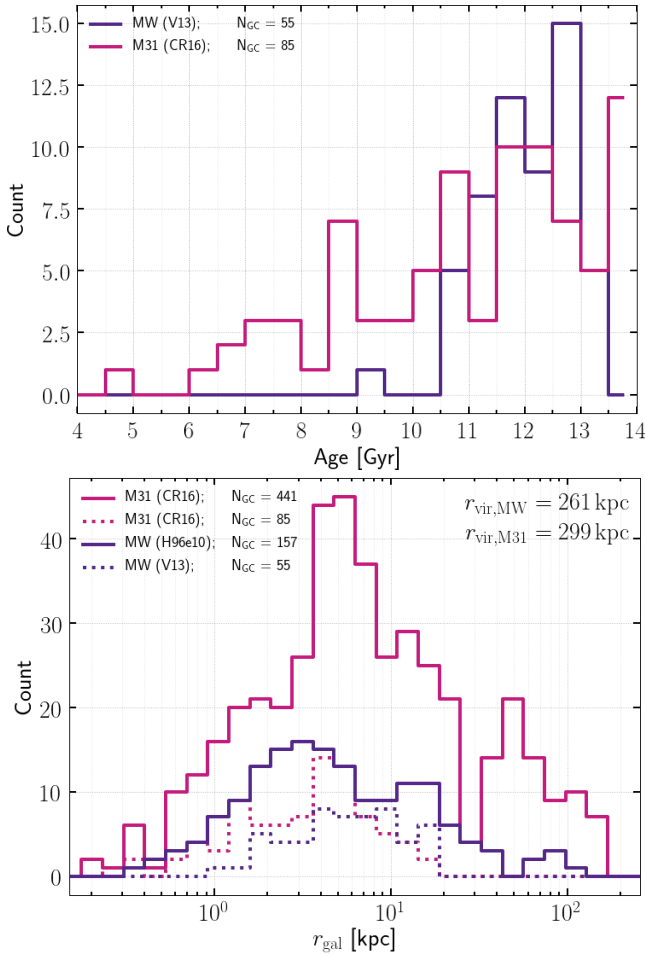
[6] https://ned.ipac.caltech.edu/

Figure 1. *Top*: Age distribution of 55 GCs in the MW (data from VandenBerg et al. 2013) and 88 GCs in M31 (data from Caldwell & Romanowsky 2016). *Bottom:* Distribution of galactocentric radius in the MW and M31. The dotted lines show the subset of data that also have age measurements (i.e. the same sample as in the top panel). We divide the radii of M31 by $r_{\rm vir,M31} = 299$ kpc and multiply by $r_{\rm vir,MW} = 261$ kpc (Patel et al. 2017) to compensate for the different intrinsic sizes of both galaxies.

Figure 2. *Top*: Mass-weighted $r_{\rm gal}$-[Fe/H] distribution of 151 GCs in the MW (data from Harris 1996, 2010 ed.), color-coded by the **median** (values also shown in each bin). The numbers in parenthesis show how many star particles fall within the bin. *Bottom*: Same for M31, showing the 366 GCs in CR16 (data from Caldwell & Romanowsky 2016). Radii of M31 are again divided by $r_{\rm vir,M31}$ and multiplied by $r_{\rm vir,MW}$. Note that the range of the colourmap differs in both figures.

lines) and find that the MW has more GCs in the range $1 - 4$ kpc than M31 (when accounting for the larger number of total GCs in M31). Interestingly, both distributions show a similar trend for $r_{\rm gal} > 4$ kpc and host a subpopulation of halo GCs. However, the two radial distributions are not statistically consistent with being drawn from the same underlying distribution due to substantial differences at intermediate radii.

3.5 Total GC mass in metallicity-radial space

We show the two-dimensional mass-weighted metallicity-radial distribution of the MW (M31) GCS in the top (bottom) panel of Figure 2. The observations indicate that no GCs with high metallicities are to be expected at large radii (the three bins in the upper right corner, both for MW and M31), and relatively few GCs at large radii in general ($r_{\rm gal} > 30$ kpc; right column: 11 GCs or 7.3% in the MW and 17 or 4.6% in M31). Moreover, the M31 hosts more metal-rich ([Fe/H]> -1) GCs in each radial bin in comparison to the MW GCSs than what would be expected when accounting for

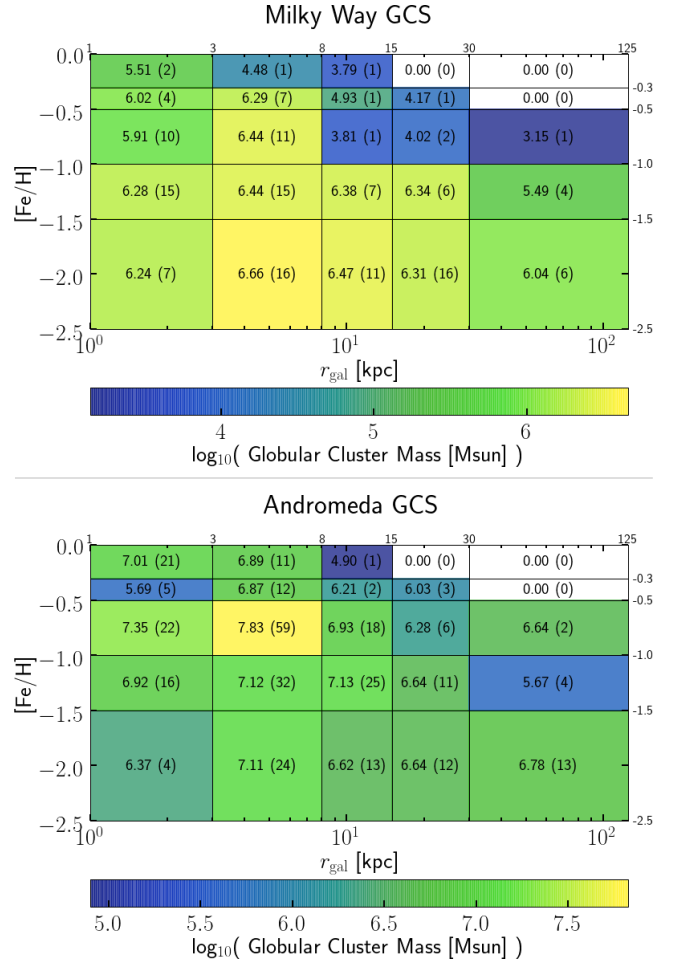the fact that M31 hosts a larger GCS than the MW. Finally, given that both marginalized (i.e. the metallicity and radial) distributions are not statistically consistent, we find that the two-dimensional distributions are also not consistent. More generally, the GCS of the MW differs significantly from that of M31. We compare these observations to the Auriga simulations later on in Sec. 4.3.

4   RESULTS

We define GC candidates in the Auriga simulations as all star particles older than 10 Gyr based on the age distribution of the MW GCS (top panel of Figure 1), and following Renaud et al. (2017).

Throughout our analysis we compare distributions of age-selected GC candidates (age > 10 Gyr) with those of all star particles (i.e. when no additional selection criterion is applied). We further split the GC candidates into an *in situ* subset (defined as GC candidates that are bound to the most-massive halo/subhalo in the first snapshot that the particle was recorded), and an accreted subpopulation (those that have formed *ex situ* and are bound to the
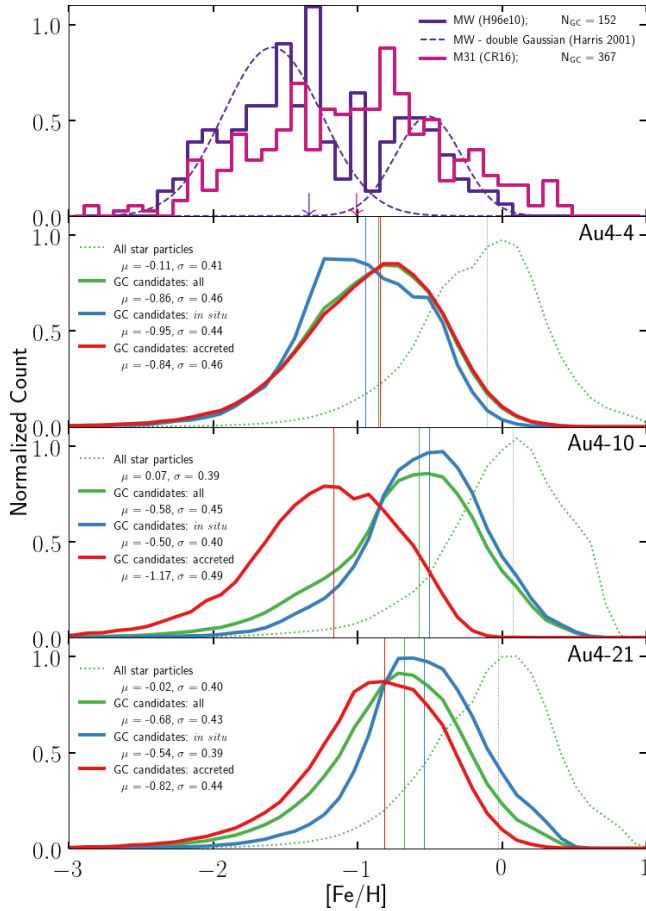
Figure 3. *Top*: Metallicity distribution of the MW and M31 GCS. The solid purple (magenta) line shows the GCSs of the MW (M31), and we indicate the mean value with an arrow at the bottom of the x-axis. We overplot a double Gaussian for the MW GCS using purple dotted lines, taking the mean and dispersion from (Harris 2001). *Other panels*: three selected Auriga haloes as indicated in the upper right corner. In each of these three panels we show the GG candidates in green, and use a green dotted line for all star particles. We split the GC candidates up into two subpopulations, those that have formed *in situ* (blue), and those that have been accreted (red).

most-massive halo/subhalo at $z = 0$). A GC candidate either formed *in situ* or it was accreted. We consider the metallicity distribution in Sec. 4.1, the distribution of galactocentric radii in Sec. 4.2, and the combination of both in Sec. 4.3.

4.1 Metallicity distribution

We investigate whether the star formation model implemented in Auriga produces metallicity distributions consistent with the MW and M31 GCSs, and whether the simulations generate sufficient total mass at metallicities typical for the MW and M31 GCSs. To visually inspect the former we show the normalized metallicity distribution of three specific Auriga galaxies in Figure 3 in comparison to the MW and M31 [Fe/H] distributions.

We select Au4-10[7], Au4-21, and Au4-4 to show the distributions of three individual simulation runs that we consider repre-
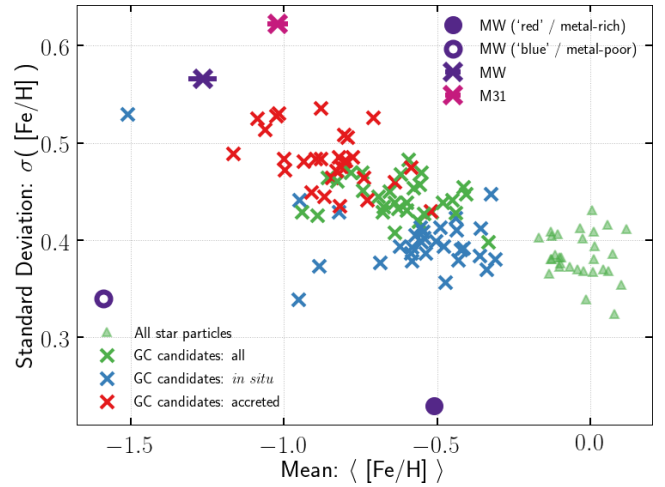
Figure 4. First vs. second central moment of the Auriga L4 metallicity distributions. Each cross (for a given colour) represents one simulation. The green (blue) [red] crosses show the values calculated using all (only *in situ*) [only accreted] GC candidates. Green triangles indicate that all stars were used. The purple (magenta) cross denotes our calculation using all MW (M31) observations (which would be appropriate for a unimodal distribution). The black solid (open) dots indicate the literature values of a bimodal Gaussian fit to the data (values from Ashman & Zepf 1998, page 38), showing the metal-rich (metal-poor) component of the MW.

sentative for specific behaviour, and to highlight that different runs could give rise to different distributions. We show the age-selected GC candidates as well as the accreted and *in situ* subsets. The top panel of Figure 3 shows the MW and M31 GCSs, where we over-plot a double Gaussian for the MW GCS by adopting literature values of the mean μ and standard deviation σ of the metal-rich and metal-poor subpopulations (Harris 2001).

We find that the age cut, on average, lowers the mean metallicity <[Fe/H]> from 0.0 to −0.6. Furthermore, accreted GC candidates generally have lower mean metallicities than the *in situ* subset with differences of roughly ∼0.3 dex for the majority of the simulation runs. This behaviour can be seen in Au4-21, while a slightly larger difference of ∼0.5 dex is seen for Au4-10 (as plotted), Au4-16, Au4-17, Au4-18 and Au4-22. However, this trend is reversed for Au4-1 and Au4-4 for which the *in situ* subset has a lower mean metallicity instead. Au4-1 is undergoing a major merger at redshift zero and we find $\mu = -1.51 (-0.74)$ for the *in situ* (accreted) GC candidates, although the former consists of only 1019 particles (1.3% of all GC candidates, and with a total mass of 5×10^7 M$_\odot$). For Au4-4, only 10.8% of the GC candidates is classified as *in situ* (compared to *in situ* fractions of 40 − 80% for other haloes). We note that Au4-4 has undergone a major merger around 2 Gyr lookback time, which is probably why the accreted population is more metal rich. After inspection of the same figure for every one of the thirty Auriga L4 haloes we find that the simulations produce (sub)populations of GC candidates that are more metal-rich than the MW and M31 GCSs. Moreover, none of the simulations produces GC candidates with a bimodal metallicity distribution.

We show the mean metallicity and standard deviation of all thirty Auriga L4 haloes in Figure 4 to illustrate the behaviour for the full set of Auriga galaxies. The green crosses are to be compared to the purple (magenta) cross, which shows the mean value of all MW (M31) GCs. In addition, we show the metal-rich (metal-poor) population of the MW GCS using a solid (open) dot. We caution

that these literature values result from individual Gaussian fits to sub sets of the observational data cut at [Fe/H] = −1. We do not include corresponding data points calculated using such an artificial cut for the simulated star particles. It is interesting that the mean metallicities of the *in situ* GC candidates appear roughly consistent with that of the metal-rich population of the MW despite the lack of such a metallicity cut, although the simulations show larger dispersions. The latter could simply be caused by the hard separation of the MW data into two groups, which means the range is smaller and the resulting dispersion lower. With regard to the M31 GCS, so far no definitive consensus has been reached in the literature concerning uni- bi- or trimodality in the [Fe/H] distribution, but CR16 argues that the data, after removal of younger objects due to improved age classification, hints at three populations separated at [Fe/H] = −0.4 and [Fe/H] = 1.5. None of the Auriga sub sets has a mean value that offers much hope that the simulated distribution is consistent with the lowest metallicity group in the M31 GCS. This is also true for the metal-poor population of the MW with a mean value of −1.6. The main result of this figure is that all Auriga L4 galaxies have metallicity distributions with (much) larger mean values than what is observed for the MW and M31 GCS, and that we systematically find lower mean metallicities for the accreted GC candidates than for those that have formed *in situ*.

We now turn to the second goal, which is to see whether sufficient total mass in GC candidates is produced by the Auriga simulations. To answer this question we plot a mass-weighted metallicity distribution in Figure 5. We show the median for all thirty Auriga L4 haloes with the 1σ interval around it (shaded regions, which shows the scatter between runs that have different initial conditions, thus, have unique merger histories). We chose to aggregate the data to indicate general trends that we find when the GC candidates are split up into the accreted and *in situ* subsets, rather than selecting typical examples of individual (simulated) galaxies. Once again we notice that the peak metallicity shifts down from [Fe/H] = 0 to [Fe/H] = −0.6 for GC candidates compared to all stars, and we find that the mass at the peak lowers by roughly one dex. The mass budget of the GC candidates is dominated by the *in situ* subpopulation above [Fe/H] = −1, and by the accreted subset below this value. We show the MW (M31) GCS in purple (magenta) and notice that the difference between the MW and M31 distributions is substantially larger than the scatter between different Auriga galaxies, particularly around [Fe/H] = −1. In addition, M31 does host (a handful of) GCs with [Fe/H] < −2.5 as well as GCs with [Fe/H] > 0 while the MW does not.

We show the ratio of the simulated to the observed profiles in the middle (bottom) panel. This mass excess can be thought of the 'mass budget' that the Auriga GC candidates can 'afford to lose' due to a combination of smaller than unity bound cluster formation efficiencies combined with a Hubble time of dynamical evolution, while still producing sufficient mass at the right metallicities. In particular, the cluster formation efficiency would have to decrease with decreasing metallicity for Auriga GC candidates to produce a population of GC candidates that is consistent with the MW. For the GC candidates in M31 we find a constant mass ratio up to [Fe/H]=−0.9, above which the simulations produce a higher mass ratio with increasing metallicity. If dynamical evolution is not expected to more efficiently disrupt GCs of higher metallicity, then we would find that the efficiency to form bound star clusters would have to decrease with increasing metallicity.
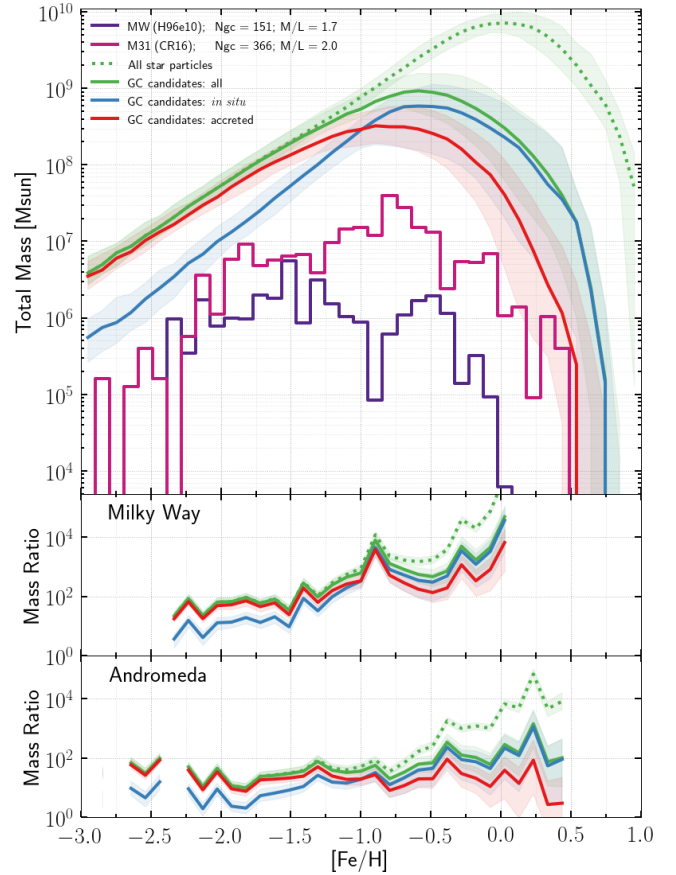

Figure 5. Mass-weighted metallicity distribution of star particles in the Auriga L4 simulations. We show the median value of all Auriga haloes for all stars (green dotted) and GC candidates (i.e. stars with age > 10 Gyr; green solid). The latter sub set is further split up between stars that formed *in situ* (blue solid), and those that were accreted (red solid). Shaded regions indicate the 1σ interval. The MW (M31) GCS is shown in purple (magenta). The middle (bottom) panel shows the ratio of the simulated mass to the mass in the MW (M31) GCS.

4.2 Radial distribution

We repeat the analysis of the previous subsection for the distribution of galactocentric radius instead of metallicity. We divide the Auriga radii by $r_{vir,Au}$ and multiply by $r_{vir,MW}$ to compensate for the different intrinsic sizes of the Auriga galaxies. We look for general trends present in all Auriga L4 galaxies. Figure 6 shows the mean and standard deviation of $\log_{10}(r_{gal})$ of star particles in all Auriga L4 simulations. The purple (magenta) cross again shows the mean of the MW (M31) GCs (which are to be compared to the green crosses), but solid (open) dot now shows our calculation of the mean value of the 'red' metal-rich ('blue' metal-poor) population. We split the radii up into the metal-rich/metal-poor groups by taking a metallicity cut at [Fe/H] = -1 as is done in the literature.

We notice that the *in situ* GC candidates are more centrally distributed, whereas the accreted subsets have a larger radial extent. This is not surprising because the classification of *in situ* requires star particles to have formed within the virial radius, thus they could naturally be expected to end up at small galactocentric radii. Accreted star particles, on the other hand, have formed in another (sub)halo beyond the virial radius, thus, they would first have to migrate inwards in order to populate the innermost radii. Moreover,
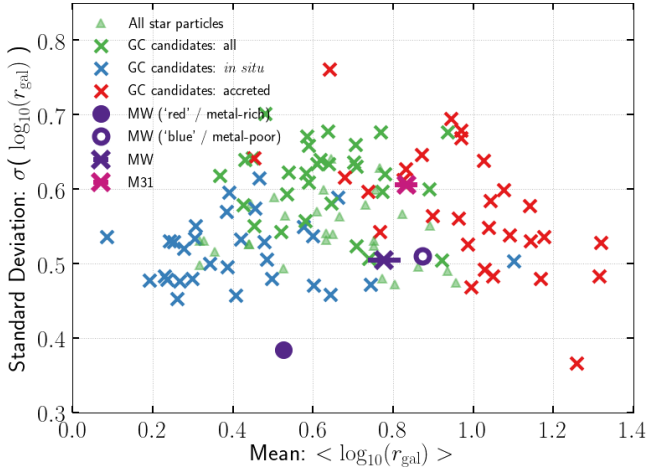
Figure 6. Mean and standard deviation of the logarithm of radial distribution of star particles in each of the thirty Auriga L4 haloes compared to the MW (M31) GCS shown in purple (magenta). The Auriga (M31) radii are divided by $r_{\rm vir,Au}$ ($r_{\rm vir,M31}$) and multiplied by $r_{\rm vir,MW}$ to compensate for different intrinsic sizes of the galaxies.

we find that the simulations have a wider dispersion in $\log(r_{\rm gal})$ than the MW GCS, while the dispersion of M31 seems to lie within the range of dispersions found in the Auriga galaxies. Furthermore, the mean of the MW GCS lies roughly within the range of values produced by the Auriga simulations, whereas the mean of M31 is somewhat larger and slightly closer to typical mean values of the accreted GC candidates in the Auriga simulations. The larger radial extent of the M31 GCS is generally believed to hint at a more accretion-dominated origin of the GCS, and may reflect a richer accretion history of M31 in comparison to the MW.

Figure 7 shows the mass-weighted radial distribution of the Auriga L4 haloes. We notice a subtle peak around 10 kpc for all star particles that is not present for the GC candidates, indicating that the stellar disc is no longer present when applying the latter selection criterion. Furthermore, we find that the dominant contribution to the total mass in GC candidates changes from those formed *in situ* to the accreted population around 10 kpc. Again we show the mass ratio of the simulations compared to the MW and M31 GCS. We find a decreasing mass ratio with increasing radius in the range 0.2 to ~5 kpc, followed by an increase attributed to the accreted subpopulation. For the MW we notice that significantly fewer GCs are found beyond 40 kpc than for M31, and that accreted GC candidates contribute mostly to the Auriga GCS at these radii. We further investigate a breakdown of the total mass in Auriga GC candidates into bins of both metallicity and radius in the following section.

4.3 Total mass in metallicity-radial space

We investigate whether the Auriga simulations still produce sufficient mass when the GC candidates are two-dimensionally binned in [Fe/H] and $r_{\rm gal}$. First we sum the total mass of GC candidates in each bin (for an individual Auriga simulation), then we calculate the median total mass in each bin over all thirty Auriga L4 haloes. The result is shown in Figure 8, which can be compared to the observed total GC mass shown in Figure 2.

To ease this comparison between the simulations and observations we take the ratio of the total mass of GC candidates in Auriga to the total GC mass in the MW (and M31). We use a diverging
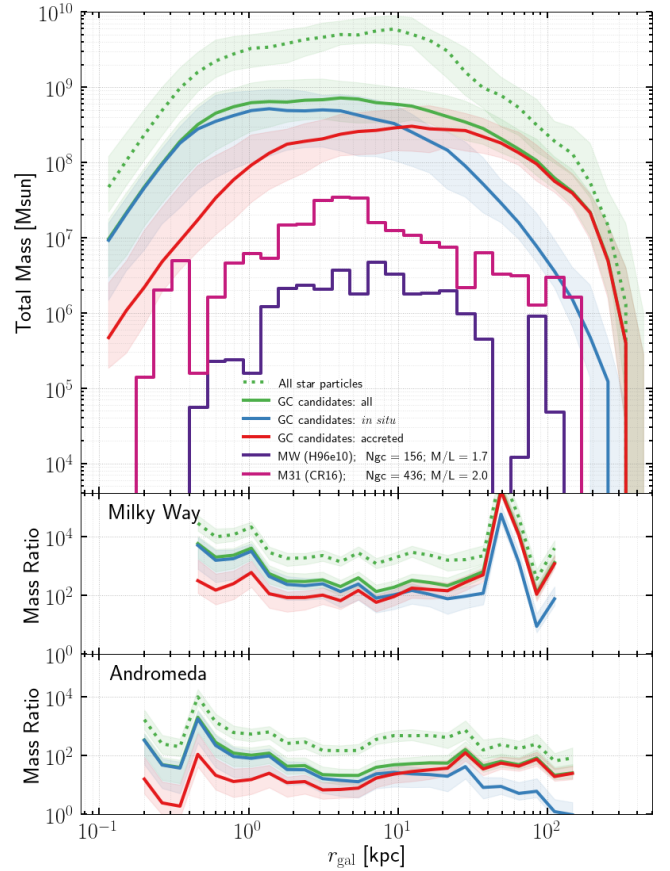

Figure 7. Mass-weighted radial distribution of star particles in the Auriga L4 simulations, where the Auriga (M31) radii are again divided by $r_{\rm vir,Au}$ ($r_{\rm vir,M31}$) and multiplied by $r_{\rm vir,MW}$. We show the median value of all Auriga haloes for all stars (green dotted) and GC candidates (i.e. stars with age > 10 Gyr; green solid). The latter sub set is further split up between stars that formed *in situ* (blue solid), and those that were accreted (red solid). Shaded regions indicate the 1σ interval. The MW (M31) GCS is shown in purple (magenta). The middle (bottom) panel shows the ratio of the simulated mass to the mass in the MW (M31) GCS.

colour map centered around the overall median of the mass ratio (i.e. we subtract the median of these twenty-five bins from the value in each bin). We show this in the top (bottom) panel of Figure 9. Note that the data in the three top right bins is masked because the mass ratio cannot be calculated due to zero mass in the observations (therefore the bins are white). If the product of the bound cluster formation efficiency and consecutive GC disruption over a Hubble time would be constant, then the value in each bin would have been zero. The red and blue bins indicate deviations from such a scenario and indicate a higher and lower than average mass excess in the simulations. The median value used to shift the mass ratio is 2.68 and 1.69 dex for the MW and M31, respectively. This means that the median 'mass budget' that the simulations 'can afford to lose' is roughly a factor 480 and 50 for the MW and M31, respectively. The lowest mass surplus for both galaxies is the bin where $-2.5 <$ [Fe/H] < -1.5 and $3 < r_{\rm gal}/{\rm kpc} < 8$, for which the simulations produce a factor $10^{2.68}/10^{1.33} \approx 22$ and $10^{1.69}/10^{0.75} \approx 9$ more mass in GC candidates than what is observed in the MW and M31 respectively. The highest factor for the MW is 2.1×10^5, and 1.1×10^3 for M31.

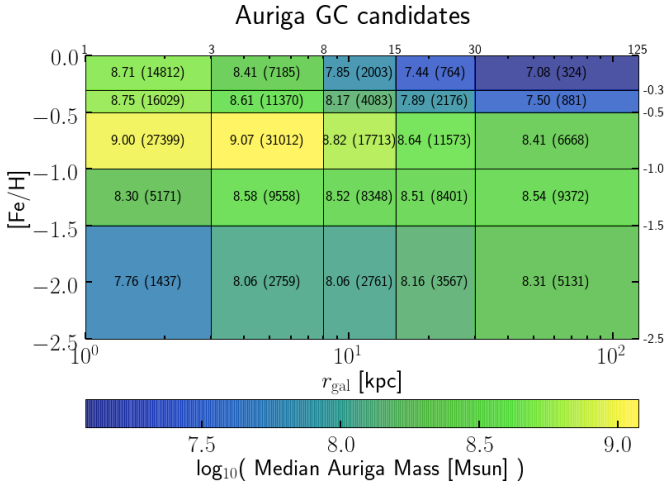We now focus on four quadrants of this diagram, split at [Fe/H] = -1 (metal-poor or metal-rich) and $r_{\rm gal}$ = 8 kpc (inside

Figure 8. Mass-weighted [Fe/H]-$r_{\rm gal}$ distribution of all thirty Auriga L4 haloes. Here we consider only the GC candidates and color-code by the median mass (values also shown in each bin). The numbers in parenthesis show how many star particles fall within the bin. Note that the range of the colourmap differs from both panels in Figure 2 (for improved contrast within the plot).

or outside the Solar radius). The majority of the mass in Auriga GC candidates is produced in metal-rich star particles inside the Solar radius. The total mass is dominated by the *in situ* component, for [Fe/H] as well as for $r_{\rm gal}$. The total mass excess in this region increases with decreasing metallicity for the MW and M31, and there is a weak trend of decreasing over-production with increasing radius for the *in situ* subsets but no trend with radius for the accreted GC candidates. As for the metal-rich GC candidates outside the Solar radius, we find that the mass excess with respect to the median is largest in this corner for the MW and M31. The main reason for this trend are the lower GC counts in the observations, whereas the Auriga simulations efficiently form metal-rich GC candidates and have no problem to produce them at large radii. The opposite is true for the metal-poor GC candidates inside the Solar radius, where the mass surplus with respect to the median is smallest for both galaxies. However, the disruption rates are expected to be particularly high for GCs in the inner regions of galaxies that are on orbits with pericentres close to the galactic bulge or bar. In addition, disk crossings in this region will cause spikes in the tidal tensor due to steep density gradients that could be highly disruptive to the GCs. The bins with the lowest 'mass budget' are in this region (a factor 9 for the MW and 22 for M31). The bound cluster formation efficiency has to exceed 10%, and none of the GC candidates in this region can experience significant mass loss in order for Auriga to produce sufficient mass in this quadrant. Finally, the metal-poor GC candidates outside the Solar radius have lower than average mass ratios, which is not surprising given that the Auriga simulations overall underproduce low-metallicity stars particles.

5   DISCUSSION

5.1   Metallicity distribution

GCs are ~0.5 dex more metal-poor than spheroid stars observed at the same radius for almost all galaxies (Harris 1991). Our selection function (age cut) does lower the mean metallicity of GC candidates by 0.5 dex with respect to all star particles, but we still find that the
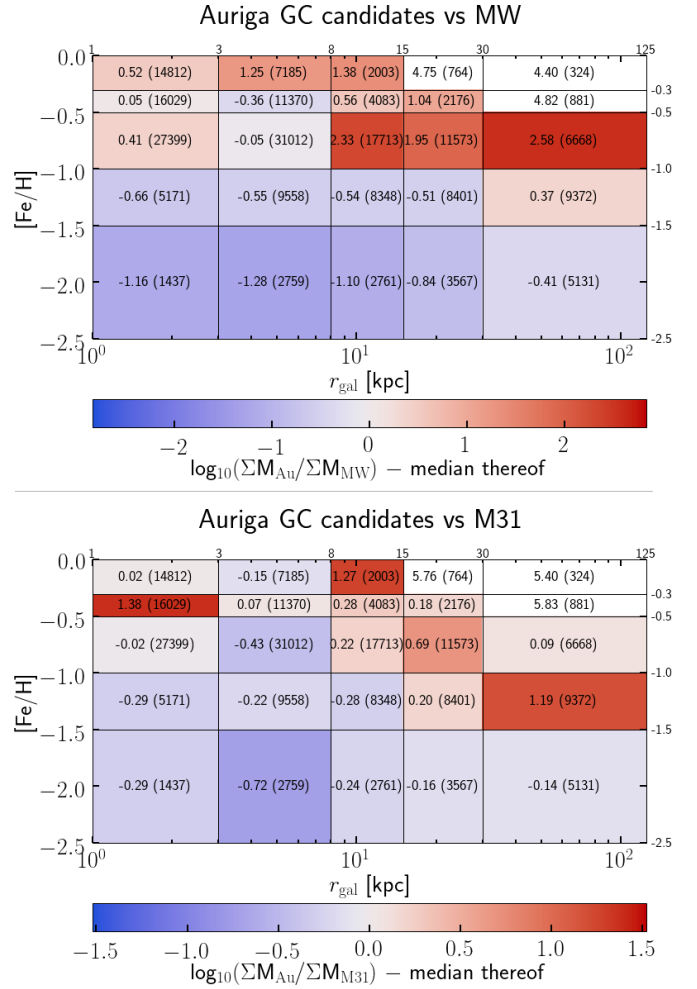

Figure 9. The top (bottom) panel shows the logarithm of the ratio of simulated mass to mass in the MW (M31) GCS, i.e. the logarithm of the mass ratio, minus the median value of these 25 bins. The values are 2.68 and 1.69 dex for the MW and M31, respectively. Red (blue) indicates a higher (lower) overall mass excess. The number in each bin shows the color-coded value that is plotted, and the (median) star particle count is given in parenthesis. Note that the three bins in the upper right corner are white because the observations have zero mass there.

GC candidates in the Auriga simulations are more metal-rich than the MW and M31 GCSs. Although the (old) star particles represent single stellar populations with a mass consistent with that of GCs, they are in fact statistical tracers of the stellar population of the galaxy as a whole. Therefore only a (small) fraction of the star particles may represent plausible formation sites of GCs, whereas the majority represents (halo) field stars - the disk component effectively falls outside our selection of star particles due to the age cut. It is implausible that all halo stars come from disrupted GCs because the total mass in GCSs at redshift zero is generally a few orders of magnitude lower than the total mass of stellar haloes of galaxies. If stellar haloes solely consist of disrupted GCs, then the GC disruption rate would have to be considerably higher than expected from theoretical models. Overall, our set of GC candidates most likely contains an overabundance of regular stars. It could be that the resulting metallicity distribution is then biased towards higher values than what is observed for real GCs. An alternative explanation could overmixing of metals at early times.

In general, the colour (metallicity) distribution of most GCSs is bimodal with typical separating value [Fe/H]~ −1 (Zinn 1985; Gebhardt & Kissler-Patig 1999; Larsen et al. 2001; Peng et al. 2006). Indeed, Ashman & Zepf (1998) and Harris (2001) find that the MW GCS has a bimodal [Fe/H] distribution. Observations of GCs in M31, however, may be best split into three distinct metallicity groups (Caldwell & Romanowsky 2016). The numerical simulation of Renaud et al. (2017) does yield a bimodal metallicity distribution where the metal-poor population is dominated by accreted star particles and the metal-rich population by *in situ* stars.

However, we find that none of the Auriga simulations produces a bimodal metallicity distribution for age-selected GC candidates. Interestingly, the cross-over point above (below) which the mass-weighted metallicity distribution of GC candidates is dominated by those that have formed *in situ* (were accreted) does coincide with the separation between the metal-rich and metal-poor populations of GCSs at [Fe/H] = −1, as for the MW. Moreover, we do find that the mean metallicity shifts when we split the GC candidates up according to birth location (accreted or *in situ*). In particular, the mean values of the *in situ* GC candidates are roughly consistent with the metal-rich MW GCs. On the other hand, we also notice that a substantial number of simulations has similar mean values for all GC candidates, and the simulated *in situ* GC candidates have larger dispersions than the metal-rich GCs. Moreover, the offset between the mean of the metal-rich and metal-poor populations in the MW is 1 dex, a factor $2 - 3$ larger than the offset that we find between the *in situ* and accreted populations. The Auriga simulations therefore do not support the view that the metal-poor GCs could have only formed in satellites that have later been accreted whereas the metal-rich GC subpopulation has only formed *in situ*. With this statement, however, we do caution that Kruijssen et al. (2019) suggests to reserve the '*ex situ*' classification for accretion after $z = 2$, when the central galaxy has formed and accretion unambiguously contributes to the radially extended halo GC population. In fact, our classification might not hold for Au4-1.

Finally, we note that Brodie & Strader (2006) compares the number of metal-poor GCs to the stellar halo mass and find[8] $T_{\text{blue}}^n \sim$ 100, while the number of metal-rich GCs compared to the bulge mass yields $T_{\text{red}}^n \sim 5$, and therefore conclude that the formation efficiency of metal-poor GCs is twenty times higher than the metal-rich GCs with respect to field stars. We find that a gradual increase in formation efficiency of GCs with respect to field stars would be required with decreasing metallicity for the GC candidates in the Auriga simulations to yield sufficient total mass to be consistent with the MW or M31 GCS. In addition, the metal-poor GC candidates would have to experience low mass loss rates, especially those within the Solar radius.

5.2 Radial distribution

The M31 GCS has a factor 2-3 more GCs at large radii compared to the MW GCS, which may indicate that M31 has a richer merger history than the MW (Caldwell & Romanowsky 2016). In the Auriga simulations we find that the GC candidates at radii larger than ∼20 kpc are indeed dominated by accreted star particles. However, we select star particles that are bound to the main halo and main subhalo, which means that we include particles up to the virial radius r_{200}. The Auriga simulations have no problem populating the stellar halo up to the virial radius, even with our additional age cut. On

the other hand, the MW and M31 have fewer GCs at large radii. We expect tidal disruption to be less efficient at larger radii, thus, the formation efficiencies of the accreted GC candidates would have to be lower. Our classification as GC candidates could especially be improved for the accreted subset. For example, we could tag only a subset of the accreted star particles as GC candidates, where the number number of GCs is determined by the satellite halo mass, given the $M_{vir} - N_{\text{gal}}$ correlation found by Burkert & Forbes (2019).

6 SUMMARY AND CONCLUSIONS

We investigate statistics of age-selected (> 10 Gyr) GC candidates in the Auriga simulations and compare the simulations to the MW and M31 GCSs. Based on our analysis we draw the following conclusions.

- The star formation model implemented in the Auriga simulations produces metallicity distributions that are more metal-rich than the MW and M31 GCSs. For most of the Auriga simulations we find that the subset of accreted GC candidates has a lower mean metallicity than the *in situ* subpopulation. However, the accreted subsets are still more metal-rich than the MW and M31 GCSs. Moreover, none of the simulated subsets has a mean metallicity as low as the mean of the 'blue' metal-poor component of the MW GCS.
- We find that the difference between the metallicity distributions of the MW and M31 GCSs is big compared to the scatter in the Auriga GC candidates of different Auriga runs. The radial distributions of the MW and M31 GCSs are somewhat more similar, but they are not consistent with being drawn from the same distribution. The scatter between the radial distributions of different Auriga simulations is smaller than the difference between the MW and M31 GCSs.
- GC candidates in the Auriga simulations may be found out to r_{200}, given that our selection function of star particles selects all stars bound to the main subhalo in the main halo. The total mass of GC candidates is dominated by accreted star particles at radii beyond 20 kpc. The GCs in the MW and M31, on the other hand, have a much smaller radial extent.
- Tidal forces are larger in the inner regions of galaxies than in the outer halo. Therefore, we expect dynamical evolution to more strongly affect GC candidates at small radii than at large radii. However, we find that the Auriga simulations produce more mass in GC candidates with high metallicities at large radii than with low metallicities at small radii. The cluster formation efficiency would have to increase with decreasing metallicity for GC candidates in the Auriga simulations to be consistent with the MW GCS. This trend of over-production of old star particles that are metal-rich and at large radii compared to observed GCs is less clear for the M31 GCS.
- Overall, we conclude that the metallicity and radial distribution of age-selected star particles in the Auriga simulations are not consistent with globular cluster system of the Milky Way or with that of the Andromeda galaxy.

---

[8] The quantity T is the number of GCs per 10^9 $M_\odot$ of galaxy stellar mass.

REFERENCES

Ashman K. M., Zepf S. E., 1992, ApJ, 384, 50
Ashman K. M., Zepf S. E., 1998, Globular Cluster Systems
Astropy Collaboration et al., 2013, A&A, 558, A33
Beasley M. A., Baugh C. M., Forbes D. A., Sharples R. M., Frenk C. S., 2002, MNRAS, 333, 383
Boley A. C., Lake G., Read J., Teyssier R., 2009, ApJ, 706, L192
Bondi H., 1952, MNRAS, 112, 195
Bondi H., Hoyle F., 1944, MNRAS, 104, 273
Boylan-Kolchin M., 2017, MNRAS, 472, 3120
Brodie J. P., Strader J., 2006, ARA&A, 44, 193
Burkert A., Forbes D., 2019, arXiv e-prints,
Caldwell N., Romanowsky A. J., 2016, ApJ, 824, 42
Caldwell N., Schiavon R., Morrison H., Rose J. A., Harding P., 2011, AJ, 141, 61
Cen R., 2001, ApJ, 560, 592
Chiou Y. S., Naoz S., Burkhart B., Marinacci F., Vogelsberger M., 2019, arXiv e-prints,
Choksi N., Gnedin O. Y., 2019a, arXiv e-prints,
Choksi N., Gnedin O. Y., 2019b, MNRAS, 486, 331
Choksi N., Gnedin O. Y., Li H., 2018, MNRAS, 480, 2343
Conn A. R., et al., 2012, ApJ, 758, 11
Côté P., Marzke R. O., West M. J., Minniti D., 2000, ApJ, 533, 869
Côté P., West M. J., Marzke R. O., 2002, ApJ, 567, 853
Diemand J., Madau P., Moore B., 2005, MNRAS, 364, 367
El-Badry K., Quataert E., Weisz D. R., Choksi N., Boylan-Kolchin M., 2019, MNRAS, 482, 4528
Fall S. M., Rees M. J., 1985, ApJ, 298, 18
Fattahi A., et al., 2019, MNRAS, 484, 4471
Faucher-Giguère C.-A., Lidz A., Zaldarriaga M., Hernquist L., 2009, ApJ, 703, 1416
Forbes D. A., et al., 2018, Proceedings of the Royal Society of London Series A, 474, 20170616
Galleti S., Federici L., Bellazzini M., Fusi Pecci F., Macrina S., 2004, A&A, 416, 917
Gebhardt K., Kissler-Patig M., 1999, AJ, 118, 1526
Gnedin O. Y., 2003, in Kissler-Patig M., ed., Extragalactic Globular Cluster Systems. p. 224 (arXiv:astro-ph/0210556), doi:10.1007/10857603_35
Gnedin O. Y., Lahav O., Rees M. J., 2001, arXiv Astrophysics e-prints,
Grand R. J. J., et al., 2017, MNRAS, 467, 179
Grand R. J. J., et al., 2018, MNRAS, 474, 3629
Gratton R. G., Carretta E., Bragaglia A., 2012, A&ARv, 20, 50
Gunn J. E., 1980, in Hanes D., Madore B., eds, Globular Clusters. p. 301
Harris W. E., 1991, ARA&A, 29, 543
Harris W. E., 1996, AJ, 112, 1487
Harris W. E., 2001, Globular Cluster Systems. Springer Berlin Heidelberg, p. 223–408, doi:10.1007/3-540-31634-5_2, https://doi.org/10.1007/3-540-31634-5_2
Harris W. E., Pudritz R. E., 1994, ApJ, 429, 177
Holtzman J. A., et al., 1992, AJ, 103, 691
Holtzman J. A., et al., 1996, AJ, 112, 416
Hunter J. D., 2007, Computing in Science and Engineering, 9, 90
Huxor A. P., et al., 2014, MNRAS, 442, 2165
Johnson T. L., et al., 2017, ApJ, 843, L21
Jones E., Oliphant T., Peterson P., et al., 2001, SciPy: Open source scientific tools for Python, http://www.scipy.org/
Kang H., Shapiro P. R., Fall S. M., Rees M. J., 1990, ApJ, 363, 488
Kim J.-h., et al., 2018, MNRAS, 474, 4232
Kovesi P., 2015, arXiv e-prints, p. arXiv:1509.03700
Kruijssen J. M. D., 2014, Classical and Quantum Gravity, 31, 244006
Kruijssen J. M. D., 2015, MNRAS, 454, 1658
Kruijssen J. M. D., Pelupessy F. I., Lamers H. J. G. L. M., Portegies Zwart S. F., Icke V., 2011, MNRAS, 414, 1339
Kruijssen J. M. D., Pelupessy F. I., Lamers H. J. G. L. M., Portegies Zwart S. F., Bastian N., Icke V., 2012, MNRAS, 421, 1927
Kruijssen J. M. D., Pfeffer J. L., Crain R. A., Bastian N., 2019, MNRAS, 486, 3134
Lahén N., Naab T., Johansson P. H., Elmegreen B., Hu C.-Y., Walch S., 2019, arXiv e-prints,
Larsen S. S., Brodie J. P., Huchra J. P., Forbes D. A., Grillmair C. J., 2001, AJ, 121, 2974
Larson R. B., 1996, in Morrison H. L., Sarajedini A., eds, Astronomical Society of the Pacific Conference Series Vol. 92, Formation of the Galactic Halo...Inside and Out. p. 241
Li H., Gnedin O. Y., 2014, ApJ, 796, 10
Li H., Gnedin O. Y., Gnedin N. Y., Meng X., Semenov V. A., Kravtsov A. V., 2017, ApJ, 834, 69
Mackey A. D., et al., 2019, MNRAS, 484, 1756
Madau P., Lupi A., Diemand J., Burkert A., Lin D. N. C., 2019, arXiv e-prints,
Marinacci F., Pakmor R., Springel V., 2014, MNRAS, 437, 1750
Marinacci F., Grand R. J. J., Pakmor R., Springel V., Gómez F. A., Frenk C. S., White S. D. M., 2017, MNRAS, 466, 3859
McConnachie A. W., Irwin M. J., Ferguson A. M. N., Ibata R. A., Lewis G. F., Tanvir N., 2005, MNRAS, 356, 979
McLaughlin D. E., van der Marel R. P., 2005, ApJS, 161, 304
Monachesi A., et al., 2019, MNRAS, 485, 2589
Muratov A. L., Gnedin O. Y., 2010, ApJ, 718, 1266
Murray S. D., Lin D. N. C., 1992, ApJ, 400, 265
Pakmor R., Springel V., 2013, MNRAS, 432, 176
Pakmor R., Marinacci F., Springel V., 2014, ApJ, 783, L20
Pakmor R., Springel V., Bauer A., Mocz P., Munoz D. J., Ohlmann S. T., Schaal K., Zhu C., 2016, MNRAS, 455, 1134
Patel E., Besla G., Sohn S. T., 2017, MNRAS, 464, 3825
Peebles P. J. E., 1984, ApJ, 277, 470
Peebles P. J. E., Dicke R. H., 1968, ApJ, 154, 891
Peng E. W., et al., 2006, ApJ, 639, 95
Perez F., Granger B. E., 2007, Computing in Science and Engineering, 9, 21
Pfeffer J., Kruijssen J. M. D., Crain R. A., Bastian N., 2018, MNRAS, 475, 4309
Portegies Zwart S. F., McMillan S. L. W., Gieles M., 2010, ARA&A, 48, 431
Recchi S., Wünsch R., Palouš J., Dinnbier F., 2017, Ap&SS, 362, 183
Renaud F., Agertz O., Gieles M., 2017, MNRAS, 465, 3622
Ricotti M., Parry O. H., Gnedin N. Y., 2016, ApJ, 831, 204
Ryu J., Lee M. G., 2018, ApJ, 863, L38

Schweizer F., 1987, in Faber S. M., ed., Nearly Normal Galaxies. From the Planck Time to the Present. pp 18–25

Spitzer L., 1987, Dynamical evolution of globular clusters

Springel V., 2010, MNRAS, 401, 791

Springel V., Hernquist L., 2003, MNRAS, 339, 289

Springel V., Di Matteo T., Hernquist L., 2005, MNRAS, 361, 776

VandenBerg D. A., Brogaard K., Leaman R., Casagrande L., 2013, ApJ, 775, 134

Vanzella E., et al., 2017, MNRAS, 467, 4304

Veljanoski J., et al., 2014, MNRAS, 442, 2929

Vietri M., Pesce E., 1995, ApJ, 442, 618

Vogelsberger M., Genel S., Sijacki D., Torrey P., Springel V., Hernquist L., 2013, MNRAS, 436, 3031

Wang S., Ma J., Liu J., 2019, arXiv e-prints

West M. J., Côté P., Marzke R. O., Jordán A., 2004, Nature, 427, 31

Whitmore B. C., Schweizer F., 1995, AJ, 109, 960

Whitmore B. C., Zhang Q., Leitherer C., Fall S. M., Schweizer F., Miller B. W., 1999, AJ, 118, 1551

Zepf S. E., Ashman K. M., English J., Freeman K. C., Sharples R. M., 1999, AJ, 118, 752

Zinn R., 1985, ApJ, 293, 424

van Rossum G., de Boer J., 1991, CWI Quarterly, 4, 283

van der Walt S., Colbert S. C., Varoquaux G., 2011, Computing in Science and Engineering, 13, 22

This paper has been typeset from a TeX/LaTeX file prepared by the author.